

Boundary effects on the Soil Water Characteristic Curves obtained from lattice Boltzmann simulations



S.A. Galindo-Torres ^{a,b,*}, A. Scheuermann ^{a,b}, L. Li ^b

^a Geotechnical Engineering Centre, School of Civil Engineering, The University of Queensland, Brisbane, QLD 4072, Australia

^b Research Group on Complex Processes in Geo-Systems, School of Civil Engineering, The University of Queensland, Brisbane, QLD 4072, Australia

ARTICLE INFO

Article history:

Received 30 June 2015

Received in revised form 18 August 2015

Accepted 18 September 2015

Keywords:

Lattice Boltzmann Methods

Unsaturated soil physics

ABSTRACT

Pore-scale simulations using a Lattice Boltzmann Method (LBM)-based numerical model were conducted to examine how the capillary pressure (P_c) and saturation (S) evolve within a virtual porous medium subjected to drainage and imbibition cycles. The results show the presence of a sharp front (interface separating the wetting and non-wetting fluids) across the cell during the test, which expectably moves up and down as the controlling non-wetting fluid pressure at the upper boundary varies to simulate different P_c levels over the drainage and imbibition cycle. This phenomenon, representing inhomogeneity at the simulated scale, is in conflict with the homogenization applied to the pressure cell for deriving the constitutive P_c – S relationship. Different boundary conditions, adopted to achieve more homogeneous states in the virtual soil, resulted in different P_c – S curves. No unique relationship between P_c and S , even with the interfacial area (A_{nw}) included, could be found. This study shows dependence of the LBM-predicted P_c – S relation on the chosen boundary conditions. This effect should be taken into account in future numerical studies of multiphase flow within porous media.

© 2015 Elsevier Ltd. All rights reserved.

1. Introduction

The Lattice Boltzmann Method (LBM) is growing in popularity for simulations of complex multiphase systems involving fluids. Since the method is based on the Boltzmann equation instead of the traditional Navier Stokes equations, it is easier to include models representing processes and effects at even the molecular scale such as those producing phase separation and immiscibility. One of the most popular models to reproduce the phase separation is by Shan and Chen (SC model) [1]. In this model, the molecular forces are included at a mesoscale by taking the average of these forces over large assemblies of particles.

The SC model has been tested with experimental data by Schaap et al. [2]. In this work, a small sub volume was simulated mainly because of the well-known, large computational intensity of the LBM. The results showed a remarkable agreement between the LBM simulations and experimental data with only minimal calibration efforts on the surface tension parameters. The pressures of the different phases were controlled by fixing the density of the components at opposite sides of the domain. Such boundary

conditions have been used afterwards in similar modelling studies (e.g., [3]). These works show that in LBM-SC simulations there is usually a front connected to the injection point of either phase. During imbibition the wetting phase invades the porous media by this front followed by pockets of fluid broken from it during drainage. During the next imbibition cycle, these pockets become connected to the front again.

The question remains whether the close link of the wetting front to the boundary conditions is a realistic feature reproduced by the LBM-SC or it is an artefact of the method. To address this question, we present here results from extensive simulations carried out to explore the dependence of the Soil Water Characteristic Curves (SWCC) simulated by the LBM-SC model on the choice of boundary conditions. The analysis focuses on the relationship between the capillary pressure (P_c) and saturation (S) of wetting fluid but also involves a third variable, the interfacial area (A_{nw}) between the wetting and non-wetting phases. Hassanizadeh and Gray [4] analysed the multiphase porous media flow system and derived a multivariate relation among the three variables: A_{nw} , P_c and S . The hysteretic cycles shown in the P_c – S curves could then be explained as projections of the P_c – S – A_{nw} relation, which forms a new basis for the constitutive soil water retention characteristic. Various studies have been carried out to validate this multivariate relation using predictions by pore-network models [5] and LBM models [3] as well as measurements from laboratory experiments [6].

* Corresponding author at: Research Group on Complex Processes in Geo-Systems, School of Civil Engineering, The University of Queensland, Brisbane, QLD 4072, Australia.

E-mail address: s.galindotorres@uq.edu.au (S.A. Galindo-Torres).

The paper is divided as follows: Section 2 explains the details of the LBM-SC implementation used for this study. Section 3 describes how the key variables used in the analysis are determined from the simulation results. The analyses for different configurations of boundary conditions are given in Section 4 followed by the discussions and conclusions in Section 5.

2. Model

For the simulations that were carried out, the LBM D3Q15 scheme [7] was chosen. In this formalism the space is divided in a cubic grid. In order to solve the Boltzmann equation, further discretization is needed in the velocity domain. For each cell, a set of 15 discrete velocities (Fig. 1) are assigned and a probability function f_i is associated with each velocity. The velocities have indexes going from 0 to 14 with the first being the rest case with null velocity. As an example the \vec{e}_{14} discrete velocity is the vector $C(1, 1, 1)$, where C is a lattice constant given by $C = \delta_x/\delta_t$ with δ_t being the time step and δ_x the side length of each square cell. To define the fluid velocity \vec{u} and density ρ at a given cell, the following relations are applied:

$$\begin{aligned}\rho &= \sum_{i=0}^{14} f_i \\ \vec{u} &= \sum_{i=0}^{14} f_i \vec{e}_i\end{aligned}\quad (1)$$

It is also important to set a weight ω_i for each direction. For the D3Q15 scheme the weights are given as follows:

$$\begin{aligned}\omega_0 &= \frac{2}{9}, \\ \omega_{i=1-6} &= \frac{1}{9}, \\ \omega_{i=7-14} &= \frac{1}{72}.\end{aligned}\quad (2)$$

After the velocities are defined, an evolution rule is implemented to solve the Boltzmann equation [8]:

$$f_i(\vec{x} + \vec{e}_i, t + \delta_t) = f_i(\vec{x}, t) + \Omega_{col}, \quad (3)$$

where \vec{x} is the position of the given cell, t is the current time step and Ω_{col} is an operator accounting for the collision of all the particles that exist within the cell. For this study, the widely accepted BGK model for the collision operator [9] was used, which assumes that

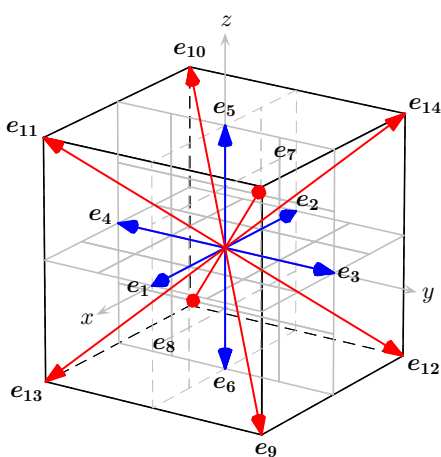


Fig. 1. LBM cell of the D3Q15 showing the direction for each of the 15 discrete velocities.

the collision processes drive the system into an equilibrium state described by an equilibrium function f_i^{eq} ,

$$\Omega_{col} = \frac{f_i^{eq} - f_i}{\tau} \quad (4)$$

where τ is a characteristic relaxation time. Further research has demonstrated that the Navier Stokes equations for fluid flow [10] are recovered if,

$$f_i^{eq} = \omega_i \rho \left(1 + 3 \frac{\vec{e}_i \cdot \vec{u}}{C^2} + \frac{9(\vec{e}_i \cdot \vec{u})^2}{2C^4} - \frac{3u^2}{2C^2} \right) \quad (5)$$

and the dynamic viscosity of the fluid ν is given by,

$$\nu = (\tau - 0.5) \frac{\delta_x^2}{3\delta_t}. \quad (6)$$

Eq. (6) imposes a constraint on the choice of τ , which must be greater than 0.5 for the viscosity to be physically correct. It has been known that values close to 0.5 produce unstable numerical behaviour [8]; hence it is always advisable to keep its value close to one.

In order to simulate multicomponent and multiphase flows as well as body forces like gravity [11], a net force is introduced for each cell. The net force \vec{F} modifies the velocity used in the calculation of the equilibrium function according to,

$$\vec{u}' = \vec{u} + \frac{\delta_t \vec{F}}{\rho}. \quad (7)$$

In the case of gravity, the force is simply $\vec{F}_g = \rho \vec{g}$ where \vec{g} is a vector representing the direction of the gravitational acceleration. Several components can also be simulated by assigning an independent lattice to each of them [12]. Then both fluid (lattices) interact by way of repulsive forces \vec{F}_r ,

$$\vec{F}_r = -G_r \rho_1(\vec{x}) \sum_{i=1}^{14} \omega_i \rho_2(\vec{x} + \delta_t \vec{e}_i) \vec{e}_i, \quad (8)$$

where G_r controls the repulsion intensity. With multiple components considered, the equilibrium velocity (Eq. (1)) must be corrected by,

$$\vec{u} = \frac{\sum_{\sigma} \sum_{i=1}^{14} \frac{1}{\tau_{\sigma}} f_i^{\sigma}}{\sum_{\sigma} \frac{\rho_{\sigma}}{\tau_{\sigma}}} \quad (9)$$

where the contribution of each component σ is accounted for [12].

The interaction of the fluids with solids is twofold. The fluids must be repelled by solid cells. Hence, the bounce-back boundary condition [8] is implemented for cells that are tagged as solids. In the bounce-back condition, after the collision step, the distribution functions are swapped symmetrically as,

$$f_{-i} = f_i \quad (10)$$

where the subscript $-i$ refers to the opposite direction to the i th velocity. However, to model capillarity effects, the fluid should also be attracted to the solid in a similar way as described in Eq. (8),

$$\vec{F}_a = -G_s \rho(\vec{x}) \sum_{i=1}^{14} \omega_i s(\vec{x} + \delta_t \vec{e}_i) \vec{e}_i, \quad (11)$$

where G_s controls the intensity of the fluid-solid attraction and the function s is unity when the neighbouring cell is tagged as solid and zero otherwise. Through parameters G_r and G_s , important quantities such as the contact angle, surface tension and immiscibility of multiple components, can be controlled. For instance the contact angle θ can be shown to follow [3],

$$\cos \theta = \frac{G_s^1 - G_s^2}{G_r} \quad (12)$$

where the superscripts indicate the different fluids.

The surface tension σ_L (in lattice units) depends on the G_r parameter in a non-linear way. The best way to determine its value is by using the Young–Laplace law,

$$P_{\text{inside}} - P_{\text{outside}} = \frac{2\sigma_L}{R} \quad (13)$$

which gives σ_L as a function of the pressure outside and inside the bubble and its radius. To find the pressure inside and outside, the following relation is used for the pressure of one cell sharing both fluids [3],

$$P(\vec{x})_L = \frac{\rho_1 + \rho_2 + G_r \rho_1 \rho_2}{3}, \quad (14)$$

with the pressure being in lattice units ($\delta_x = \delta_t = C = 1$). Fig. 2 shows bubbles of two different sizes simulated as well as the results indicating a linear relation between the pressure difference and the inverse of the radius.

To convert the pressure into real physical units P_p , the following formula is used [3],

$$P_p = \frac{\sigma_L}{\sigma_p \delta_x} P_L \quad (15)$$

which uses the value of the surface tension measured in lattice and physical units with the value of the grid size in physical units to obtain the proportionality constant needed for the conversion. To finalize the description of the model, Table 1 shows the parameter values used in the model. It is important to note that although the densities for both fluids are equal, this discrepancy with the experimental case can be disregarded as demonstrated in Ref. [2].

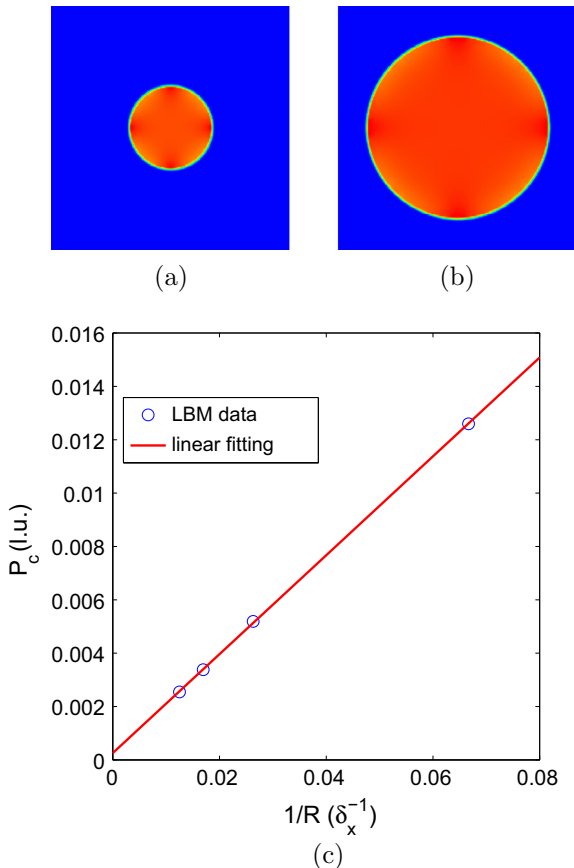


Fig. 2. Bubble simulations of a lighter fluid (red) inside the denser one (blue) for two different radii: (a) $20 \delta_x$ and (b) $70 \delta_x$. (c) Linear relation between the pressure difference (in lattice units) and the inverse of the radius. (For interpretation of the references to colour in this figure legend, the reader is referred to the web version of this article.)

Table 1
Parameters values used in the simulations.

Parameter	Value
δ_x	10^{-4} m
τ	1.1
G_r	1.0
G_s	$\pm 0.5^a$
ρ_0 , equilibrium density for both fluids	1.0 g/cm^3
σ_p	0.028 N/m

^a The sign differentiates the wetting and non-wetting fluids.

3. Upscaling variables and equilibrium condition

There are 3 main variables that are quantified and analysed in this study, namely: the capillary pressure P_c , the saturation S of wetting fluid and the interfacial area A_{nw} . To determine these three variables requires the identification of the volumes occupied by the different fluids. With the multicomponent LBM as described in the previous section, both fluids co-exists in a given cell but with different densities. Therefore a threshold value must be defined to differentiate the volumes of the fluids. The threshold is set to be half the initial density. Fig. 3 shows a square grid that has been processed in this way.

Once the volumes are identified, the key variables are determined. The simplest one is the saturation S , which can be determined as the number of cells in the wetting fluid volume divided by the number of non-solid cells (total void cells). To determine P_c , the pressure is calculated independently at each cell using Eq. (14). Then the pressure of each phase is determined by the average pressure of the cells belonging to the enclosed volumes. We have observed some variance in the distribution of pressure within the fluid specially when there are individual fluid pockets disconnected from the main front. However in the situations where this study are focussed on, there is a clear front of connected fluid and small variance for the average pressure. Once this average is obtained, the difference gives the value for P_c . Although the pressures are controlled at the boundaries, the boundary pressure values are not representative of the pressure values within the LBM domain. In fact they can be quite different mainly because of the variance in densities within the sample. Finally for the interfacial area, the *isosurface* function of MATLAB was used. Once the triangular mesh enclosing one of the volumes is obtained, the surface area is determined by the addition of the triangles areas. This gives the surface area enclosing the volume occupied by each fluid (A_w for the wetting fluid and A_n for the non-wetting fluid). These surface areas contain contact surfaces with solids but A_{nw} includes only the area of the interfaces separating both fluids. To obtain A_{nw} from A_w and A_n , the following formula is used [6],

$$A_{nw} = \frac{A_w + A_n - A_s}{2}, \quad (16)$$

where A_s is the surface area of the solids. It is important to remember that the definition of A_{nw} is per void volume and thus it has unit of mm^{-1} .

To construct a complete P_c – S curve, 100 simulations were carried out for each model configuration with the boundary non-wetting fluid pressure increased or decreased (according to the imbibition or drainage cycle) incrementally over a large range that corresponds with the whole saturation range. Under each preset pressure, the simulation ran for 5000 iterations (LBM time steps) to ensure that the system reached the equilibrium state for the SWCC analysis, i.e., P_c and S becoming invariant. This was validated by re-running the simulations with doubled number of iterations. As shown in Fig. 4), a larger number of iterations did not lead to any considerable changes of the results, which suggests that for

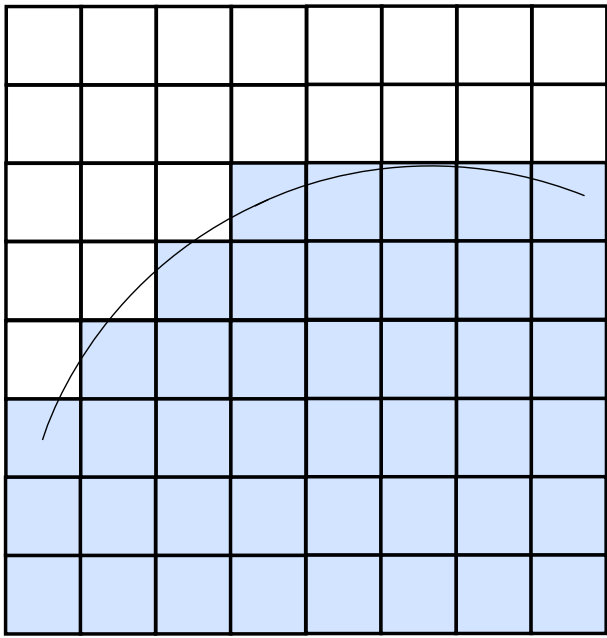


Fig. 3. LBM cells are classified according to the fluid they contain the most. The colours signal different fluids. A line is drawn to divide both volumes. The line, or surface in 3D, can be obtained from an iso-surface algorithm. (For interpretation of the references to colour in this figure legend, the reader is referred to the web version of this article.)

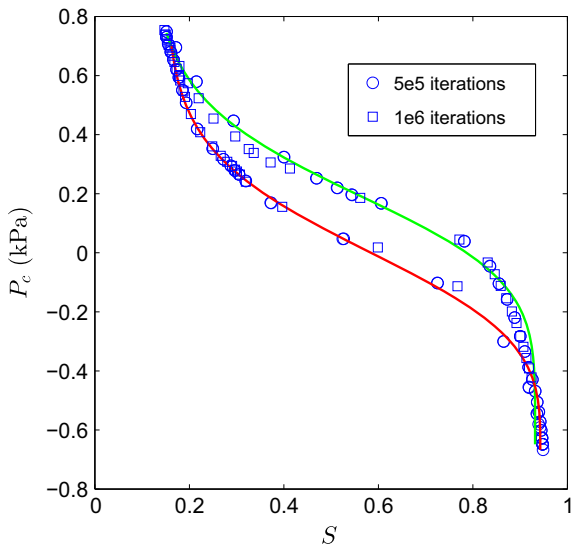


Fig. 4. Equilibrium test showing a consistent $P_c - S$ curve obtained from simulations using different numbers of iterations. The solid lines are added for visual aid.

both sets of simulations, equilibrium conditions were attained. Therefore, 5000 iterations were sufficient and applied in all the simulations presented here.

4. Dependence of simulated $P_c - S - A_{nw}$ relation on boundary conditions

4.1. Uniform boundary conditions

The simulated porous medium was made of spherical particles of a uniform size, packed in regular and irregular arrays within a cubic pressure cell. The initial regular packing combined with the

neglect of the gravity force ensures the symmetry of the problem with respect to the axes so that the study can be focused on the different boundary and flow conditions. As explained in the previous section, the pressure of the non-wetting fluid is changed at the boundaries in sequence to gradually increase and decrease the P_c level to simulate the drainage and imbibition cycle, respectively. The simulation continued until the steady state condition was reached for each value of P_c .

In the first case (called 1D hereafter), the simulation was based on a 1D configuration with wetting and non-wetting fluid pressures set on two opposing boundaries respectively as shown in Fig. 5(c). This is similar to the set-up of a pressure cell standard device used to measure the $P_c - S$ curve (see Fig. 5(a)). This is a widely used design to measure the SWCC [13] where the boundary conditions are the same as in the 1D case. Snapshots of the simulated fluid distributions at different stages (P_c level) of the simulation are shown in Fig. 6. Note that these are equilibrium results. During drainage, the non-wetting fluid invaded the porous medium with a pattern of tubular structures moving through the channels (connected pore space) formed by the regular sphere packing. Clear separation between the wetting and non-wetting fluids across the cell was evident. During imbibition of the wetting phase, the separation of the two fluids at the cell scale became even more profound, with a relatively uniform, flat interfacial geometry. A video of animated simulation results included in the [Supplementary material](#) shows these changes in sequence. The standard 1D set-up according to the pressure cell results in a sharp front separating the wetting and non-wetting fluids across the simulation domain/device, which is strongly linked with vertical fluid flows during the transient state in response to changes of the non-wetting fluid pressure on the top boundary.

The analysis led to the SWCC as shown in Fig. 7, where the primary drainage and imbibition curves are fitted with the Van Genuchten (VG) function [14]. To show the bounds set by the primary curves, several scanning curves (similar $P_c - S$ drainage and imbibition curves but with smaller P_c ranges) obtained from simulations with different limit values of P_c are also plotted. Overall these simulated water retention curves are in qualitative agreement with experimental observations, including the non-zero and non-unity limits of S , which reflect the trapped residual contents of wetting and non-wetting fluid towards the end of drainage and imbibition, respectively (Fig. 6).

In the second case (called 3D hereafter), pressure boundary conditions are applied to the six faces of the cubic domain (Fig. 5(d)). These conditions replace the no flow boundary conditions on opposing four faces adopted in the first case. Three adjacent faces control the pressure for the wetting phase and the remaining three faces control the pressure of the non-wetting phase. As shown in Fig. 8, the change of the boundary conditions led to different fluid distributions from those simulated in the 1D case at all stages of the drainage and imbibition cycles. The non-wetting fluid coming from the three controlling faces merged close to the corners, eliminating the tubular structures during drainage (which was evident in the 1D case). The flatter/smooth front in the 3D case would result in a lower interfacial area A_{nw} for the same saturation during drainage.

The SWCC curves were also determined for the 3D case simulation. The primary drainage and imbibition curves were found to differ significantly from those for the 1D case (Fig. 9(a)). The 3D case exhibits a smaller hysteresis loop area. The lower limits of the wetting fluid saturation are also very different between the two cases, showing how the amount of the fluids trapped within the cycles depends on the boundary conditions. To further examine the upscaling of the $P_c - S$ relation, the interfacial area per void volume (A_{nw} in units of mm^{-1}) between the wetting and non-wetting

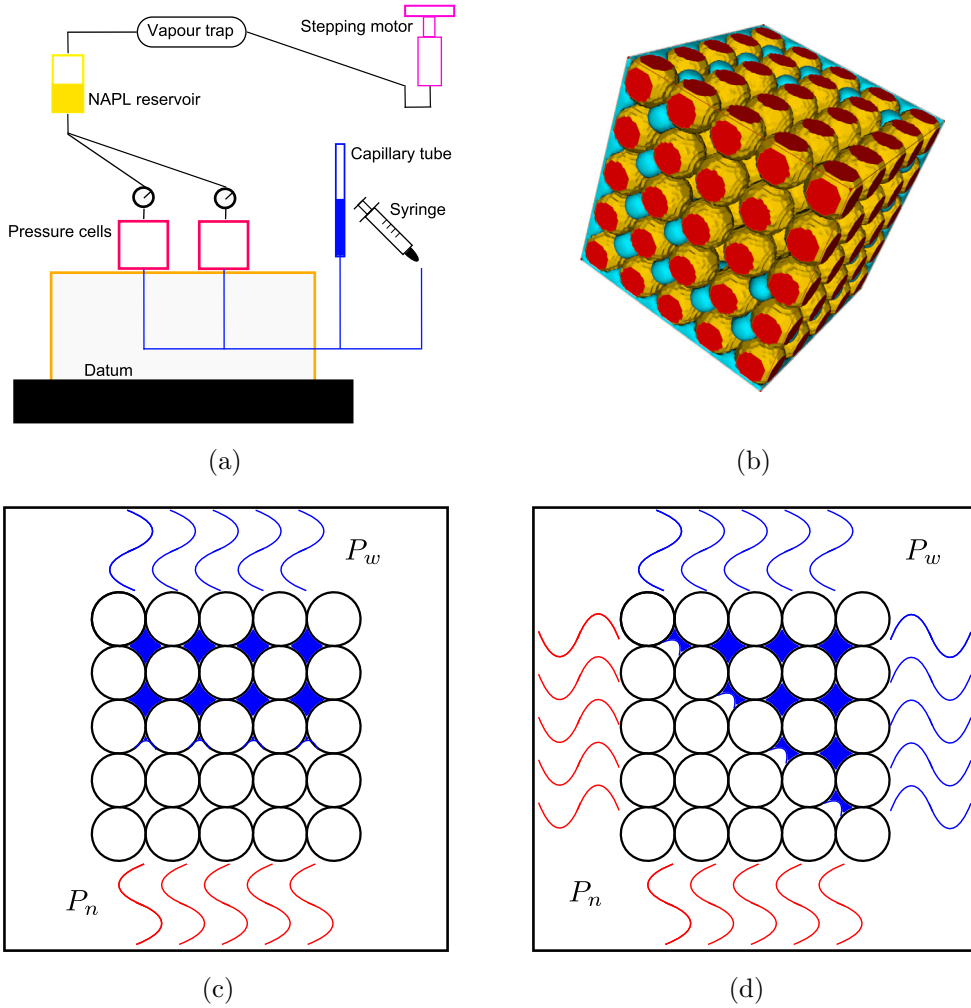


Fig. 5. (a) Shows a typical pressure cell where water and air enter from opposite sides. (b) Shows the LBM model configuration for the standard pressure set-up with a regular array of spheres representing the granular material. For the purpose of convenience, a cubic cell is simulated with a 1 cm side length and grains with a diameter of 2 mm. The results from the simulation show clearly the presence of a sharp front across the cell with the standard set-up. In the figure only the non-wetting phase is shown for the case with the standard cell set-up. (c) and (d) Shows that different boundary conditions applied to a pressure cell produce different wetting fronts, even for the same saturation of 50%, potentially leading to different SWCC.

fluids was also determined from the simulation results. As described previously, cells forming the interface between wetting and non-wetting fluids were identified and subsequently meshed with a triangular tessellation to facilitate the calculation of the interfacial area. Fig. 9(b) shows the measured area for the two cases with different boundary conditions. The tubular structure evident in the snapshots shown in Fig. 6 produced a large interfacial area during drainage in the 1D case while the more homogeneous 3D condition presented a small variation in the interfacial area between the two main cycles.

As discussed in the introduction, the multivariate P_c-S-A_{nw} relation has been assumed to represent the porous medium's intrinsic property, taking a unique form with hysteresis incorporated. This relation was also examined based on the simulation results. The P_c-S-A_{nw} data were fitted with a second order bi-dimensional polynomial function for the 1D and 3D case, respectively. The fitting results were satisfactory with very high regression coefficients obtained for both cases (Fig. 9(c)). However, the fitted functions differed significantly between the two cases, as shown by the surfaces plotted in Fig. 9(c) and fitted coefficient values of the functions. No unique P_c-S-A_{nw} relation could be found. Attempt was also made to fit all the data with a single

function; however, the result was far from satisfactory with a very low regression coefficient value, indicating scatters in the data and non-unique P_c-S-A_{nw} relation between the cases.

4.2. Non uniform boundary conditions

To explore the effect of the front formed in the simulations for both cases in relation to this non-unique P_c-S-A_{nw} behaviour, we modified the boundary conditions to avoid net flows in any particular direction. The cube faces were divided equally into a number of squares where alternating wetting and non-wetting fluid pressures were specified (Fig. 10(a)–(d)). Four cases were considered with different numbers of square divisions. Both fluids, being equally injected into or pushed out of the cell from all sides, experienced zero net flow in all directions. As a result, the front became fragmented with smaller length scales than the size of the domain. The system became increasingly more homogeneous across the domain with the length scale of the front decreasing as the number of square divisions on the boundaries increased (Fig. 10(e)–(h)).

The SWCCs obtained from the simulations for the four additional cases also showed different P_c-S behaviours (Fig. 11(a))

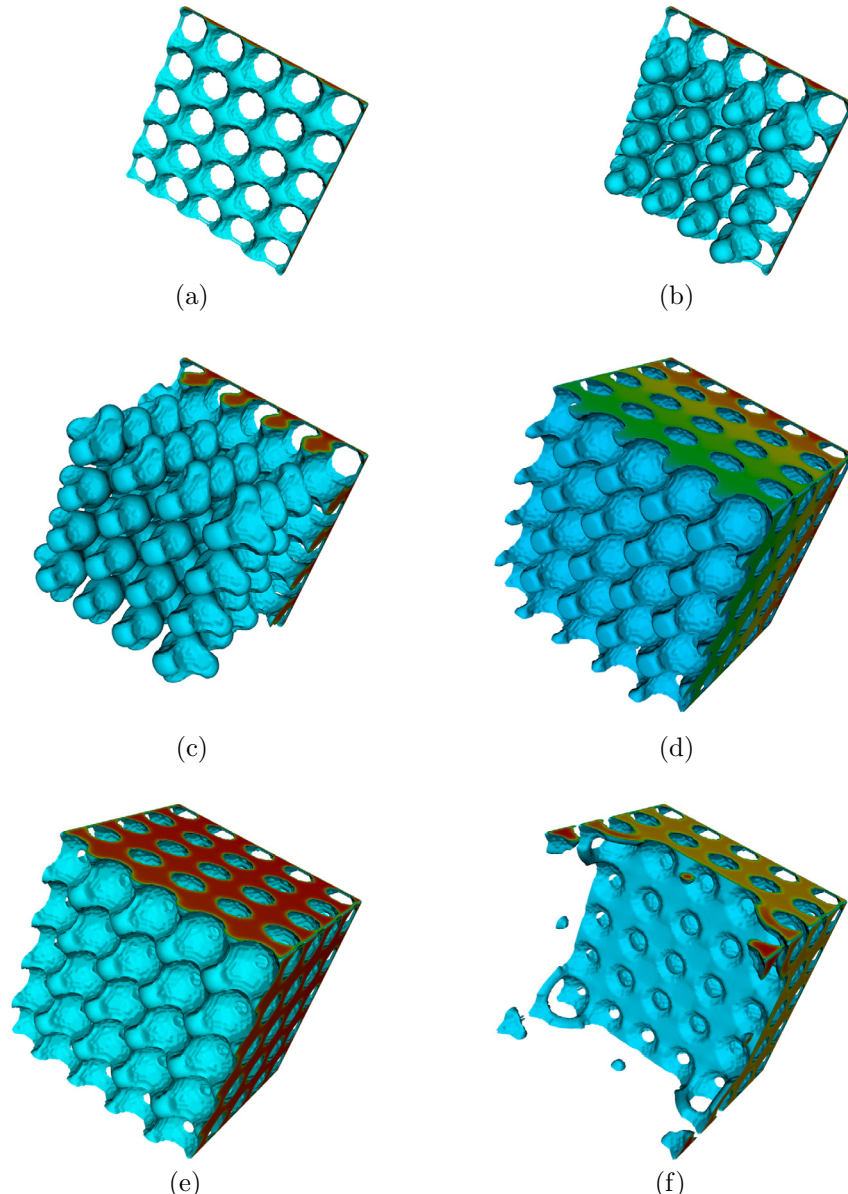


Fig. 6. Snapshots of simulated, equilibrium fluid distributions at different stages of drainage (a–c) and imbibition (d–f) for the 1D case. The solid and wetting phases are hidden, and only a mesh representing the non-wetting phase is shown for clarity. A tubular structure is evident during imbibition, which increases the interfacial area as discussed below.

from the results based on the standard 1D set-up, particularly in the lower saturation limit. The boundary condition in the standard set-up permitted more complete drainage of the wetting fluid to a low saturation near zero. In contrast, large residual wetting fluid contents were found during drainage for the new cases, especially those with 25 and 100 square divisions on the boundaries. In these cases, as can be seen from the video in the [Supplementary material](#), the wetting fluid became disconnected from the boundaries, leading to accumulation of water in the middle of the domain. The disconnection of the wetting phase from the boundaries prevented the non-wetting fluid from completely invading the pore space and hence led to high residual wetting fluid contents. Increasing further the value for P_c produced numerical instability due to the high compression that both fluids were subjected to. While the case with 4 square divisions behaved differently, the cases of 25 and 100 squares produced very similar SWCC, suggesting some kind of converged behaviour. However, whether this

behaviour represents the constitutive P_c – S relation of the system remains a question.

The A_{nw} results show larger interfacial areas in these cases with modified boundary conditions compared with the standard set-up, for the same water saturation in the domain ([Fig. 11\(b\)](#)). The interfacial area increased with the number of square divisions on the boundaries, indicating the effect of reduced front scales. The results also show similar behaviour of the A_{nw} – S relation for the last two cases with division number equal to 25 and 100. The hysteretic differences between drainage and imbibition appeared to be smaller in the cases with modified boundary conditions compared with the 1D case.

4.3. Soil randomly distributed

A further analysis was carried out in a similar soil but with a random structure to ascertain that the observed effects are not

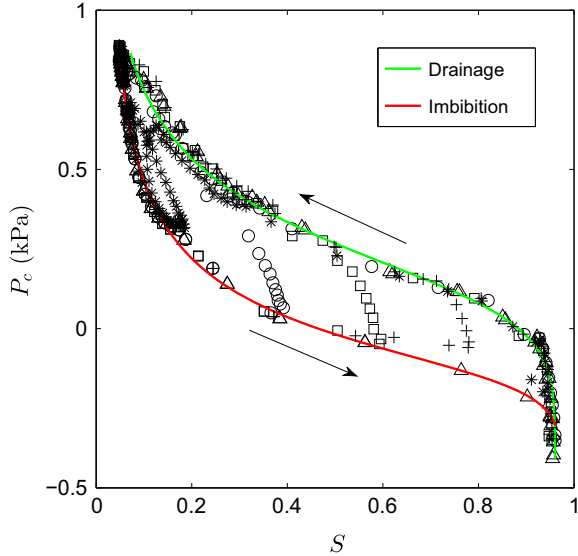


Fig. 7. SWCC for the 1D case showing the drainage and imbibition curves fitted with the VG model. The different symbols show results from simulations of different scanning curves. The arrows indicate the progression of the drainage and imbibition cycle.

due to the highly organized soil structure simulated. The porosity is slightly lower in the random soil (0.40 compared with 0.43 in the regular soil). The same 1D and 3D boundary conditions are imposed over the domain. Fig. 12 shows different snapshots of the results for each boundary condition. These results show that the fluid is distributed in a more random way with more disconnected pockets after each imbibition and drainage cycles. There is no longer a tubular structure like that shown in the previous case, which explains the large difference in the interfacial area compared with previous cases (for the regular soil).

Fig. 13 shows the different variables plotted for the 1D and 3D cases. The P_c - S curves are now narrower for both cases but the dependence of the P_c - S relation on the boundary conditions are clearly evident in the simulations with the random soil. The limit values for P_c are smaller compared to the cases with the regular soil. This indicates an increased capillary effect on the wetting of the porous medium due to its lower porosity and pore size, which in turn reduces the value of P_c required to fully drain the medium. The dependence of the P_c - S - A_{nw} relation on the boundary conditions remains evident in the difference of the results between the 1D and 3D cases. The boundary effect seems to be less pronounced due to the absence of tubular structures during the imbibition of the non-wetting phase seen in the regular soil cases.

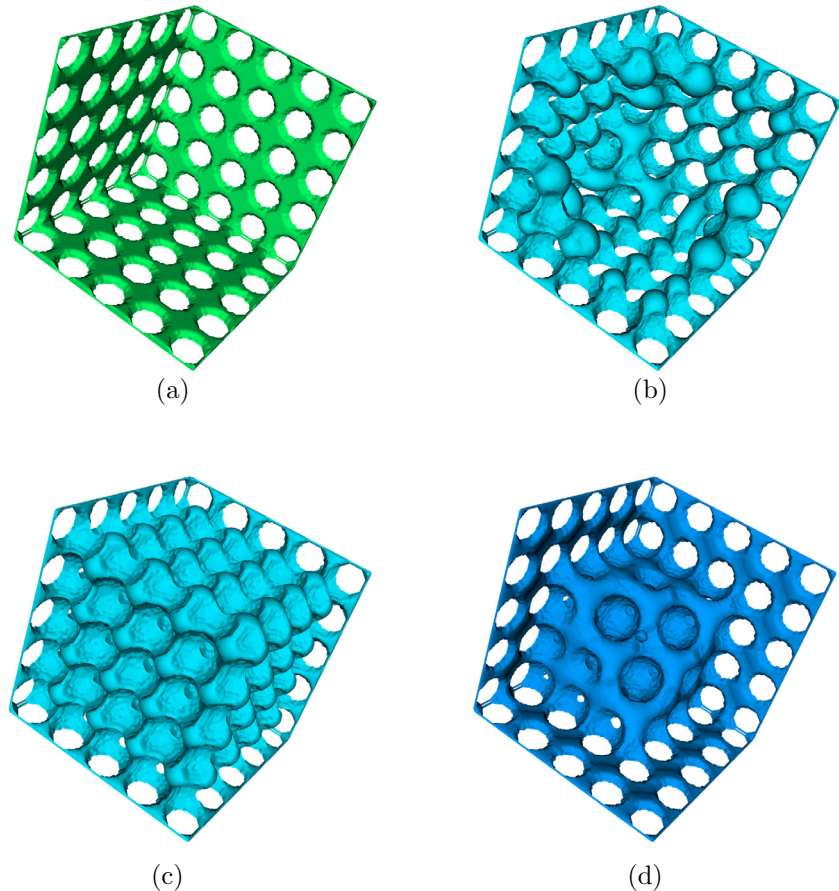


Fig. 8. Snapshots of simulated, equilibrium fluid distributions at different stages of drainage (a and b) and imbibition (c and d) for the 3D case. The solid and wetting phases are hidden, and only a mesh representing the non-wetting phase is shown for clarity.

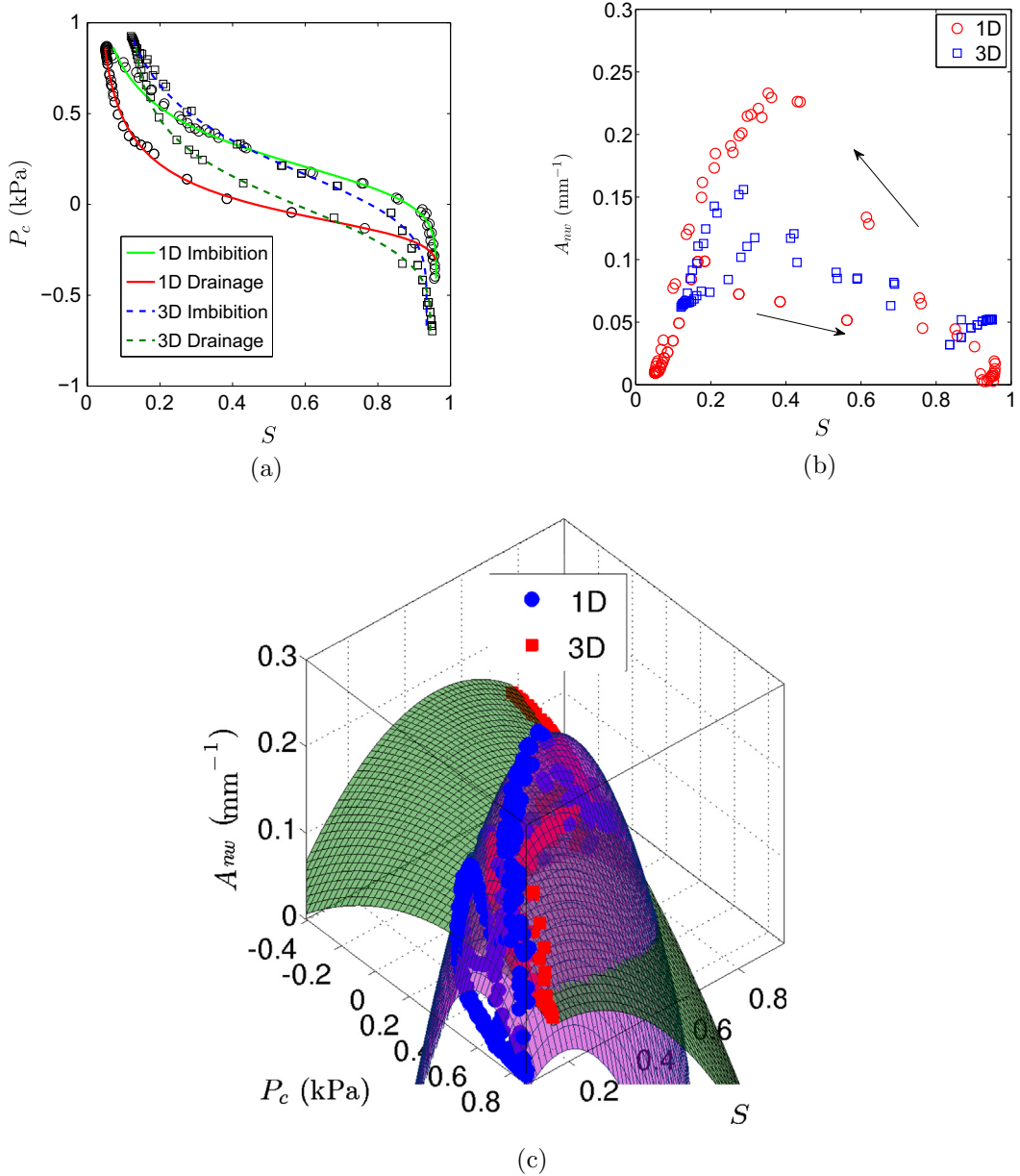


Fig. 9. (a) Comparison of the SWCCs for the 1D and 3D cases. (b) Comparison of the A_{mw} vs S relation. (c) Comparison of the P_c – S – A_{mw} relation, fitted with a parabolic function.

5. Discussion and concluding remarks

The SWCC, applied in continuum models as a porous medium's intrinsic property, is assumed to be a unique constitutive relation, especially when the interfacial area is also incorporated in the formulation to account for hysteresis. The presented results have demonstrated that LBM-SC simulations cannot deliver such a unique relation with the grid sizes that are commonly used.

The results show that the process underlying the SWCC is the redistribution of wetting and non-wetting fluids in the porous medium as the amounts of both fluids increase and decrease correspondingly. This redistribution process is linked to the flow during the transient state controlled by the boundary conditions. The standard set-up leads to a vertical transient flow and distinct distributions of both fluids separated by a single front across the domain. The numerical model with modified boundary conditions simulated more homogeneous fluid distributions with fronts (fluid separation) occurred at smaller scales and predicted different

P_c – S – A_{mw} relation, particularly with larger interfacial areas but smaller hysteretic difference between the drainage and imbibition cycles (compared with the results given by the standard set-up). The P_c – S – A_{mw} relation depends on the way that drainage or imbibition takes place as affected by the boundary conditions. These relations were further explored with a random soil packing. Again differences of the simulated P_c – S – A_{mw} relation remained as a result of different boundary conditions applied to the simulation domain.

The uniqueness of the SWCC has been challenged previously by evidences showing its dependence on mechanical soil properties [15] and flow rate imposed on the boundaries [16]. To the best of the authors knowledge, it is the first time that evidence, numerical at this point, is presented on how the boundary conditions and more generally the flow conditions affect the fluid distribution in the porous medium within a testing cell and hence the measured SWCC. Further studies should be carried out to verify this non-uniqueness experimentally or find a true Representative Element

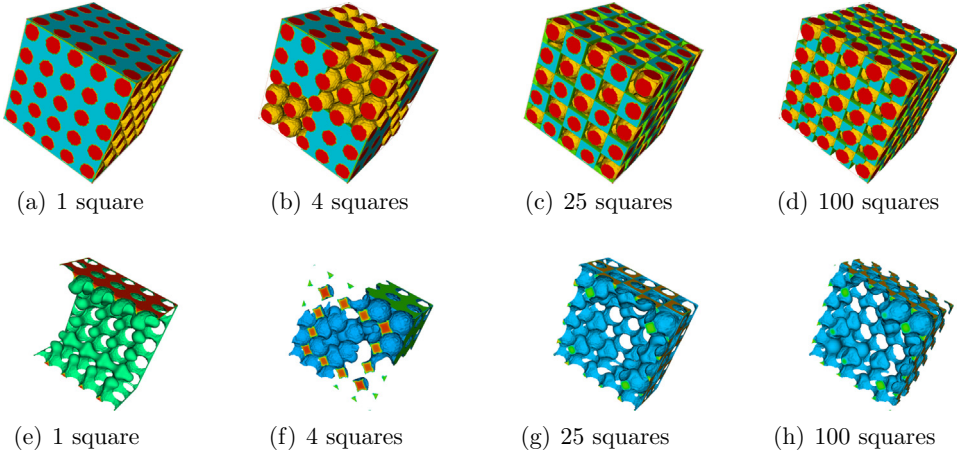


Fig. 10. (a)–(d) Four different boundary conditions. The faces of the cube are divided in equal square areas with alternating injection of wetting and non-wetting fluids. In the last three cases, the same number of injection squares are introduced for both phases. The only exception is the first case where 4 faces contain the non-wetting fluid with the remaining 2 injecting the wetting phase. (e)–(h) Different snapshots of the four cases showing how the fluid front becomes fragmented and how the fluid distribution strongly depends on the boundary conditions.

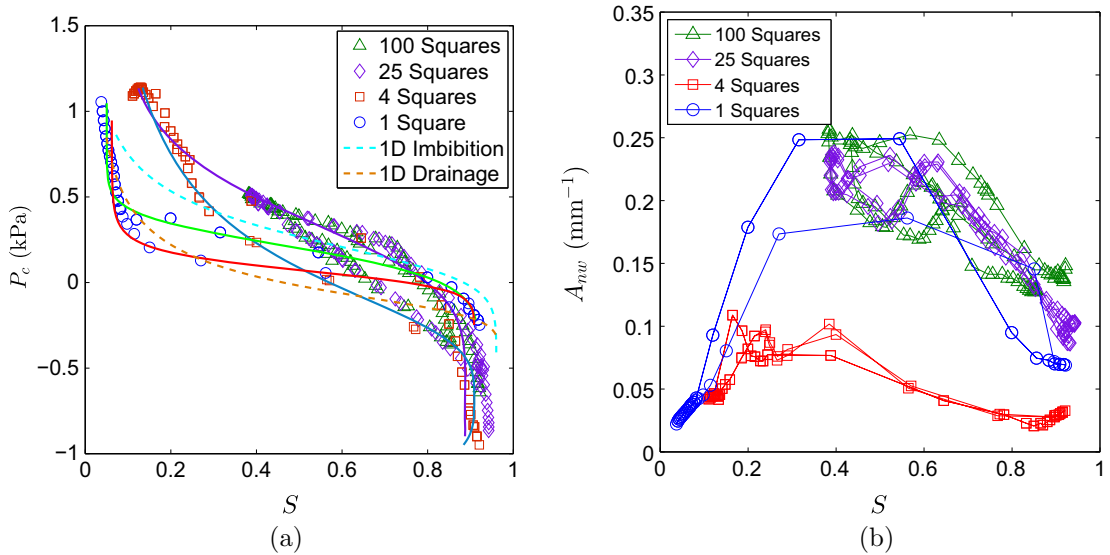


Fig. 11. (a) SWCCs for the four cases with modified boundary conditions illustrated in Fig. 10. The main cycles are fitted with the VG function for the first two cases only. The VG fitted for the 1D case of Fig. 7 is also shown for comparison. (b) Interfacial area A_{nw} as a function of saturation. A line is drawn between consecutive points to help visualize the point sequence.

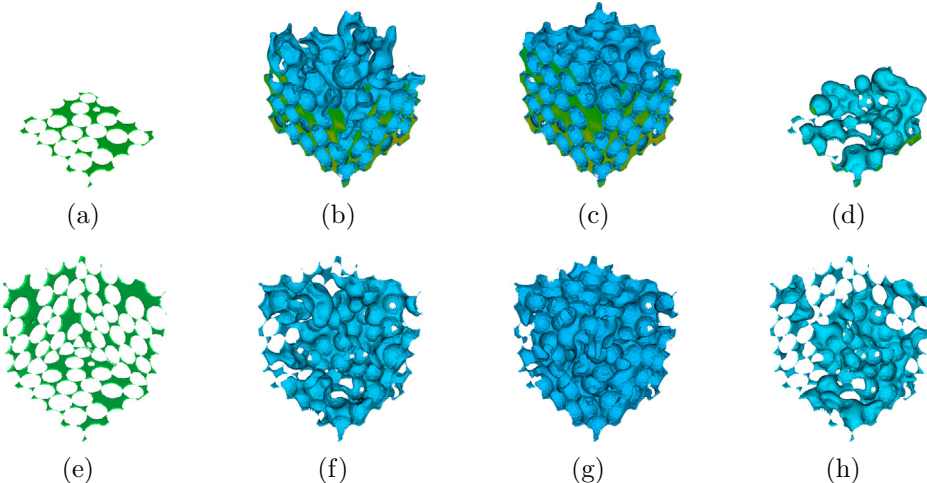


Fig. 12. Snapshots of simulated, equilibrium fluid distributions at different stages of drainage and imbibition for both the 1D (a–d) and 3D (e–h) cases within the random soil. The solid and wetting phases are hidden, and only a mesh representing the non-wetting phase is shown for clarity.

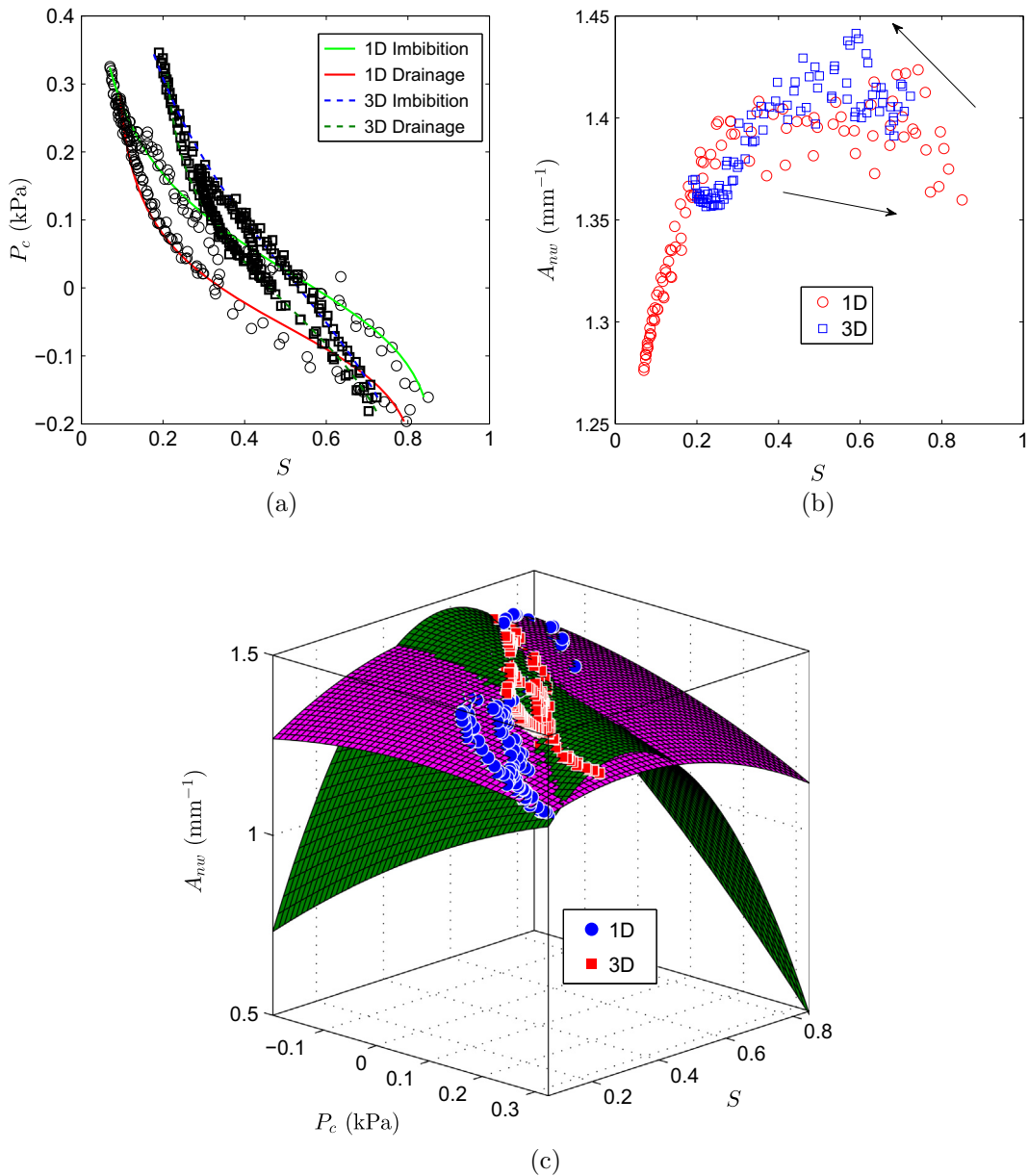


Fig. 13. (a) Comparison of the SWCCs for the 1D and 3D cases in the random soil. (b) Comparison of the A_{nw} vs S relation. (c) Comparison of the P_c – S – A_{nw} relation, fitted with a parabolic function.

Volume for the LBM simulations, which, as shown by this work, may be considerably larger than previously expected.

Acknowledgements

This work was funded by the ARC Discovery project (DP140100490) Qualitative and quantitative modelling of hydraulic fracturing of brittle materials. The first author also wants to acknowledge the support from the University of Queensland Early Career Research Award (RM2011002323). The simulations were carried out using the Mechsys open source library on the Macondo high performance computing cluster of the University of Queensland.

Appendix A. Supplementary data

Supplementary data associated with this article can be found, in the online version, at <http://dx.doi.org/10.1016/j.comgeo.2015.09.008>.

These data include MOL files and InChiKeys of the most important compounds described in this article.

References

- [1] Shan X, Chen H. Lattice Boltzmann model for simulating flows with multiple phases and components. *Phys Rev E* 1993;47:1815–9. <http://dx.doi.org/10.1103/PhysRevE.47.1815>.
- [2] Schaap M, Porter M, Christensen B, Wildenschild D. Comparison of pressure-saturation characteristics derived from computed tomography and lattice Boltzmann simulations. *Water Resour Res* 2007;43(12):W12S06.
- [3] Porter ML, Schaap MG, Wildenschild D. Lattice-Boltzmann simulations of the capillary pressure saturation interfacial area relationship for porous media. *Adv Water Resour* 2009;32(11):1632–40. <http://dx.doi.org/10.1016/j.advwatres.2009.08.009>. URL <<http://www.sciencedirect.com/science/article/pii/S0309170809001328>>.
- [4] Hassanizadeh S, Gray WC. Mechanics and thermodynamics of multiphase flow in porous media including interphase boundaries. *Adv Water Resour* 1990;13(4):169–86. [http://dx.doi.org/10.1016/0309-1708\(90\)90040-B](http://dx.doi.org/10.1016/0309-1708(90)90040-B). URL <<http://www.sciencedirect.com/science/article/pii/030917089090040B>>.
- [5] Joekar-Niasar V, Hassanizadeh S, Leijne A. Insights into the relationships among capillary pressure, saturation, interfacial area and relative permeability

- using pore-network modeling. *Transp. Porous Media* 2008;74(2):201–19. <http://dx.doi.org/10.1007/s11242-007-9191-7>. URL <<http://dx.doi.org/10.1007/s11242-007-9191-7>>.
- [6] Culligan KA, Wildenschild D, Christensen BSB, Gray WG, Rivers ML, Tompson AFB. Interfacial area measurements for unsaturated flow through a porous medium. *Water Resour Res* 2004;40(12):n/a–a. <http://dx.doi.org/10.1029/2004WR003278>. URL <<http://dx.doi.org/10.1029/2004WR003278>>.
- [7] Galindo-Torres S. A coupled discrete element lattice Boltzmann method for the simulation of fluid solid interaction with particles of general shapes. *Comput Methods Appl Mech Eng* 2013;265(0):107–19. <http://dx.doi.org/10.1016/j.cma.2013.06.004>.
- [8] Sukop M, Thorne D. Lattice Boltzmann modeling: an introduction for geoscientists and engineers. Springer Verlag; 2006.
- [9] Qian Y, d'Humieres D, Lallemand P. Lattice BGK models for Navier–Stokes equation. *EPL (Europhys Lett)* 1992;17:479.
- [10] He X, Luo L. Lattice Boltzmann model for the incompressible Navier–Stokes equation. *J Stat Phys* 1997;88(3):927–44.
- [11] Martys NS, Chen H. Simulation of multicomponent fluids in complex three-dimensional geometries by the lattice Boltzmann method. *Phys Rev E* 1996;53:743–50. <http://dx.doi.org/10.1103/PhysRevE.53.743>.
- [12] Shan X, Doolen G. Multicomponent lattice-Boltzmann model with interparticle interaction. *J Stat Phys* 1995;81(1):379–93.
- [13] Drake SS, O'Carroll DM, Gerhard JI. Wettability contrasts between fresh and weathered diesel fuels. *J Contam Hydrol* 2013;144(1):46–57. <http://dx.doi.org/10.1016/j.jconhyd.2012.09.008>. URL <<http://www.sciencedirect.com/science/article/pii/S0169772212001301>>.
- [14] Van Genuchten MT. A closed-form equation for predicting the hydraulic conductivity of unsaturated soils. *Soil Sci Soc Am J* 1980;44(5):892–8.
- [15] Malaya C, Sreedep S. Critical review on the parameters influencing soil–water characteristic curve. *J Irrigat Drain Eng* 2012;138(1):55–62. [http://dx.doi.org/10.1061/\(ASCE\)IR.1943-4774.0000371](http://dx.doi.org/10.1061/(ASCE)IR.1943-4774.0000371).
- [16] Wildenschild D, Hopmans J, Simunek J. Flow rate dependence of soil hydraulic characteristics. *Soil Sci Soc Am J* 2001;65(1):35–48.